Energy 236 (2021) 121449

Contents lists available at ScienceDirect

Energy

journal homepage: www.elsevier.com/locate/energy

Mortar dynamic coupled model for calculating interface gas exchange between organic and inorganic matters of shale

Gaohui Cao [a], Wenbin Jiang [a, b, *], Mian Lin [a, b, **], Lili Ji [a], Zhipeng Xu [a, b], Siping Zheng [a, b], Fang Hao [c]

[a] Institute of Mechanics, Chinese Academy of Sciences, Beijing, 100190, China
[b] School of Engineering Science, University of Chinese Academy of Sciences, Beijing, 100049, China
[c] School of Geosciences, China University of Petroleum, Qingdao, Shandong, 266580, China

ARTICLE INFO

Article history:
Received 20 January 2021
Received in revised form
6 July 2021
Accepted 7 July 2021
Available online 14 July 2021

Keywords:
Shale gas
Dynamic transport
Interface exchange
Mortar

ABSTRACT

Shale gas has revolutionized the world energy in recent years. In this work, a mortar dynamic coupled model (MDCM) is successfully built for simulating gas transport from molecular motion in nanopores to highly permeable fractures. Results show that the production duration of MDCM can reach about tenfold that of a single medium model, which affords a microscale explanation for the long tail production. We also propose a two-stage process in the variation of the mass-exchange-rate with the pressure difference of organic matter and inorganic matter: it is nonlinear in Stage I, while shows a linear relationship in Stage II. Combined with theoretical analyses, numerical simulations and dimensional analyses, an efficient and practical relation for calculating the interface gas exchange in tail production is obtained. The relation offers a valuable tool for the gas transport properties in fractured shale and is finally validated by a gas expansion experiment. Better performance can be obtained in terms of accuracy and precision than the current model. These results stress the need for a change of paradigm from statistic to dynamic *trans*-scale transport. The new insights into transport in the long-term shale gas production suggest new leads for the industry.

1. Introduction

Natural gas, an important energy sources governing the world economy [1,2], accounts for approximately 24% of global energy consumption in 2018 and will increase to about 30% by 2060 [3]. U. S. Energy Information Administration (EIA) estimates that in 2020, U. S. natural gas accounts for 34% of primary energy consumption, and shale gas accounts for about 86% of total natural gas production. The rapid development of horizontal drilling and hydraulic fracturing has opened up vast reservoirs of shale gas for cost-effective production. The share of shale gas will continuously increase as the depletion of conventional gas and oil resources through 2050. The extraction of shale gas has evoked unprecedented effect on macroeconomic, notably in energy structure and energy prices [4]. Despite the increasing role of shale gas in today's energy market, key questions remain including the environmental concerns (such as CO_2 emission [5]) and the long term extraction efficiency. In fact, the increased availability of shale gas, which produces roughly half the CO_2 than coal for the same heat output, helps US emissions falling to 1990 levels [6]. As for the extraction efficiency, production rate of shale gas usually peaks within the first few months and then declines rapidly followed by a long tail. This unique feature of the exploration increases the volatility in the supply part. Improving the accuracy of prediction of shale gas production, could massively increase shale gas extraction efficiency and reduce the environmental footprint of shale gas production. The modeling of shale gas production serves as an important foundation for prediction.

In 2017, through extensive data mining and analysis of 23 years of production from 20,000 wells in Barnett Shale, researchers in Los Alamos National Laboratory found that shale gas production is actually dominated by long-term tail production rather than the high-profile initial rapidly-declining production in the first 12

* Corresponding author. Institute of Mechanics, Chinese Academy of Sciences, Beijing, 100190, China.
** Corresponding author. Institute of Mechanics, Chinese Academy of Sciences, Beijing, 100190, China.
E-mail addresses: jiangwenbin@imech.ac.cn (W. Jiang), linmian@imech.ac.cn (M. Lin), haofang@cug.edu.cn (F. Hao).

https://doi.org/10.1016/j.energy.2021.121449
0360-5442/

months [6]. Earlier in 2013, Patzek et al. [7] have proposed a scaling theory and explained the tai production by interference of hydraulic fractures. However, in 2016, Lee et al. [8] found that recovery is hampered by interfacial effects at the wet kerogen surface, they proposed a two-regime decline: a short time decay is consistent with Darcy description, followed by a fast algebraic decay resulting from increasingly unreachable energy barriers. Later, Chen [9] found that the tail production is controlled by the interaction between a fast and a slow transport mechanism of inorganic matter (IOM) and organic matter (OM) within shale reservoirs. The mechanical mechanism of the long tail of shale gas production is still under debate. Which factor in which scale, or their combined effect, controls tail production is unclear. It is therefore imperative to establish a deep scientific understanding of the typical multiscale phenomenon, which is indeed a challenging task because of the nonlinear dynamics of the interfacial effects, the non-Darcy flow, as well as the adsorption and desorption processes.

Shale reservoirs have strong heterogeneity, and gas transports in a complex multi-scale system [10,11]. So far considerable efforts have been devoted to establish connections at different scales. From the electronic scale, the density functional theory method in quantum mechanics is used to calculate the interation between graphene and methane [12,13]. On the nano-scale, molecular dynamics (MD) is widely applied to model gas flow and adsorption in the nanopores of shale [14]. However, as the number of particles increases, it is impossible to give all the initial conditions of the particles, fortunately, statistical physical method and kinetics have been formed [15] to describe the phase space distribution. On the micro-scale, pore network model is an effective technique for the permeance of shale gas, as it accounts for the actual geometry of the porous networks [16,17]. Typically, shale gas reservoirs consist of a collection of kerogen pockets, the host nanoporous OM containing the hydrocarbons, distributed throughout the mineral shale rock. In IOM, hydraulic fractures cooperated with natural fractures construct fast channels for shale gas transport. While in OM, gas flow in nanopores, which has significant nonlinear effects such as adsorption/desorption, diffusion, and slippage [18–20]. OM, which is highly dispersed in IOM and has no global connectivity, releases its hydrocarbon content as the pressure in the fracking fractures is decreased. The dual-porosity transport model has been widely used to describe transport processes within porous media consisting of two subdomains [9,21,22]. A linear relationship between the exchange flow rate and the pressure difference between OM and IOM is assumed in the previous studies. The interfacial effect is simulated in such a simple way. However, whether this assumption is true or not is worth exploring, and the established relations also contain some coefficients difficult to be determined. In our previous works [23,24], a coupled model of OM and IOM for calculating the apparent permeability for organic-rich shale is proposed. The advantage of this method is that it realizes the upscaling of static parameters such as permeability and porosity. However, gas production is actually a dynamic process. The reliability of the macroscopic results obtained by the upscaling methods for static parameters contains significant uncertainties. However little, if any, research has focused on upscaling for dynamic transport. In fact, the importance of the dynamics of linear and non-linear systems is noticed in many fields [25,26]. A better understanding of the dynamic characteristics of the microscale shale gas transport is the basis for *trans*-scale researches and critical to accurately predicting gas production and to improve extraction efficiency while reducing environmental impacts.

Overall, the mechanical mechanism of the long tail remains essentially not understood. The most heavily contested point is which factor dominates tail production in the complex multiscale flow. The main objective of this work is to develop a dynamic coupled method, which takes into consideration the effects of various mechanisms, such as the interfacial effects, the non-Darcy flow, the adsorption processes and the geometry of the nanoporous networks, to improve the so far limited scientific understanding.

This study is the first study that puts insight into the interface mass exchange between OM and IOM by microscale coupled simulation. The main contribution of this study to the literature is that the detailed microscale dynamic process of shale gas flow and its contribution to tail production. Here, we present an in-depth theoretical study of gas transport from nanoporous OM to fractured IOM. Combining theoretical analyses, numerical simulations and dimensional analyses, we also provide a semi-analytical expression for the interface gas exchange, which allows to rationalize hydrocarbon transport in shale and quantitatively describe the permeance from OM to IOM. Despite the intrinsic complexity of such heterogeneous, multiscale porous media, the interface gas exchanges are shown to follow a simple dimensionless relation with the permeability ratio and porosity ratio. The relation offers a valuable tool for the gas transport properties in fractured shale and is finally validated by experiments. The flow chart of this study is shown in Fig. 1.

2. Mortar dynamic coupled model

Shale gas flows in a multi-scale system (Fig. 2). The macro-scale multi-stage horizontal well fracturing causes a complex coupled system of OM and IOM in SRV (stimulated reservoir volume). OM is highly dispersed in IOM and the flow mechanisms of them are quite different. When focused on the micro-scale, gas exchange between the organic pore network and the inorganic fractures, and the methane in the OM is an important source of shale gas. To understand the micro-scale dynamic transport mechanism for tail production, a mortar dynamic coupling model is proposed in this study, as shown in Fig. 2. Despite its simplicity, this robust model captures the main physical ingredients at play in hydrocarbon extraction from nanoporous OM through its external interface towards the fractured IOM. This is key to gaining fundamental understanding of the mechanism of tail production at play.

In MDCM, OM is modeled by pore network model (PNM), and IOM is modeled by finite volume method (FVM). In OM, the non-Darcy effect is assigned (covers viscous flow, slip flow, Knudsen diffusion and adsorption) and the adsorption parameters are obtained by MD calculation (nano-scale MD calculation provides the theoretical basis and physical images for the transformation of free gas phase and adsorbed gas phase). In IOM, a homogeneous porous medium is hypothesized where gas flows in natural and hydraulic fractures. At the interface of OM and IOM, Mortar method is adopted for interface coupling. Mortar method allows considering different physical mechanisms and using different mathematical models in the subdomains which are most suitable for them. And Mortar coupling can enforce pressure and flow continuity even if the pores and fractures on the subdomains are not connected directly. It is an effective method for the OM-IOM coupled system with strong heterogeneity in shale.

2.1. OM

OM is modeled by PNM. OM is responsible for the generation of hydrocarbons during the thermal maturation of source rocks. This geochemical process engenders a network of organic pores. PNM abstracts the pore space of porous media as a network connected by pores and throats and thus is effective to account for the geometry of the nanoporous OM (See Fig. 3). Commonly used constructing methods for pore networks include the methods based on

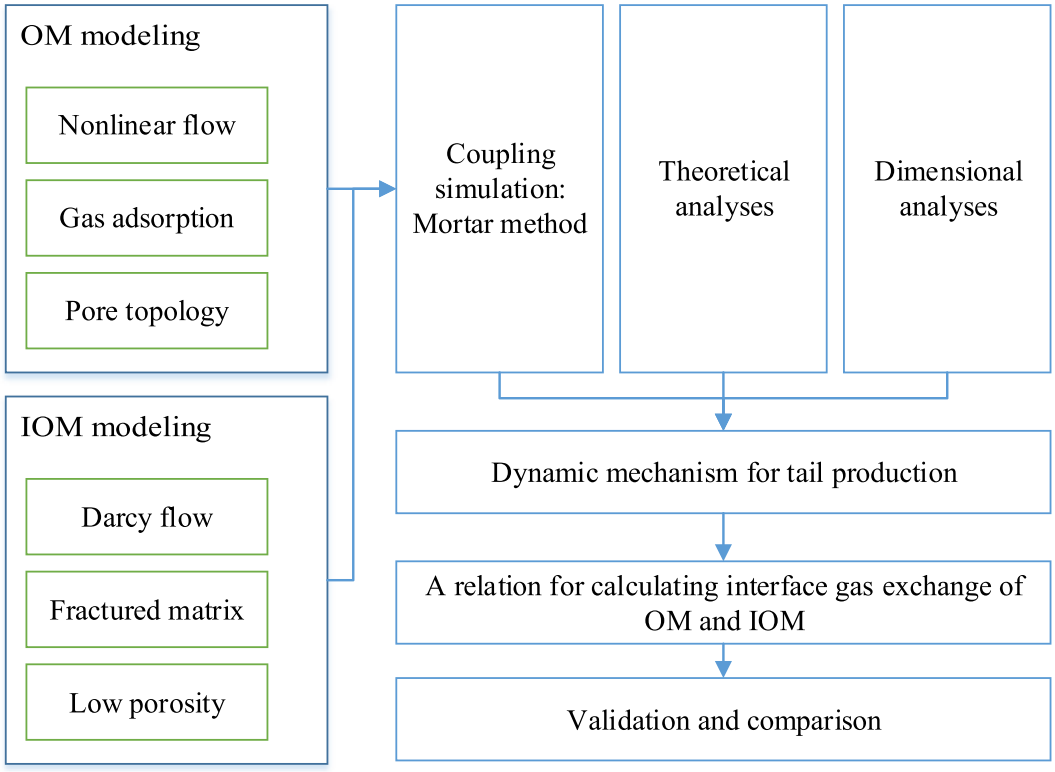

Fig. 1. Flow chart of this study.

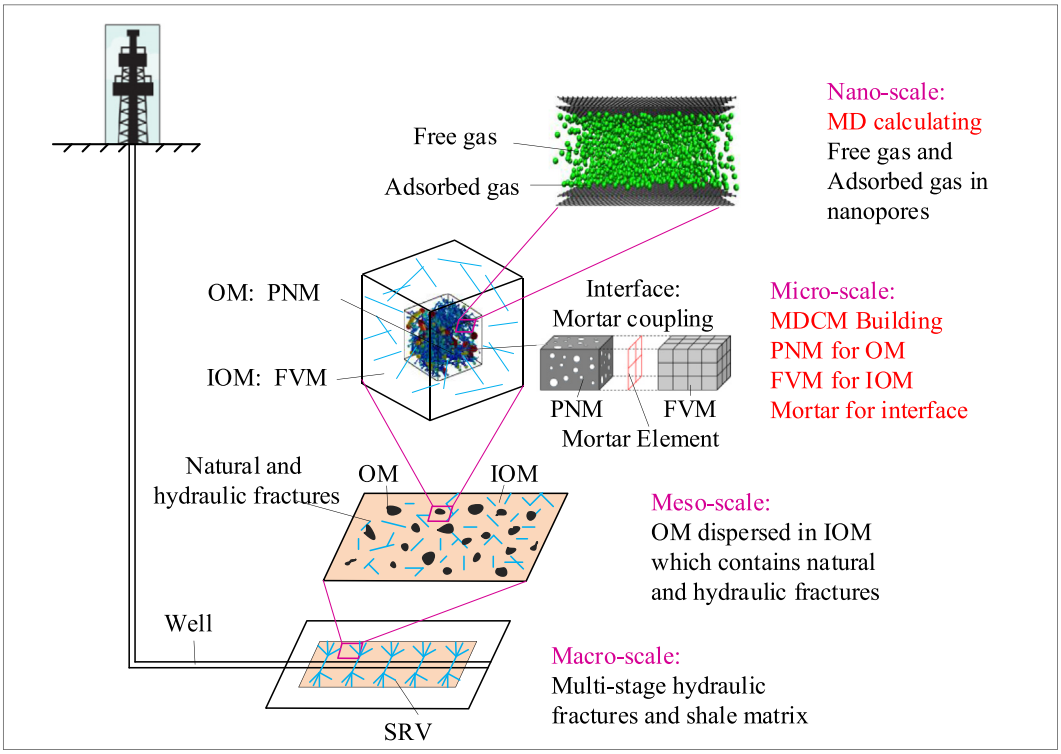

Fig. 2. Multi-scale shale gas transport and MDCM establishment.

distribution parameters [27] and based on scanned images [28,29]. In this work, a random pore network based on important parameter distributions (pore radius distribution, throat radius distribution, coordination number distribution) is applied at first. Thus OMs with different distribution parameters are studied, making the consideration of OM more universal. In addition, a PNM extracted from scanning images is also build for a real shale sample to validate the method.

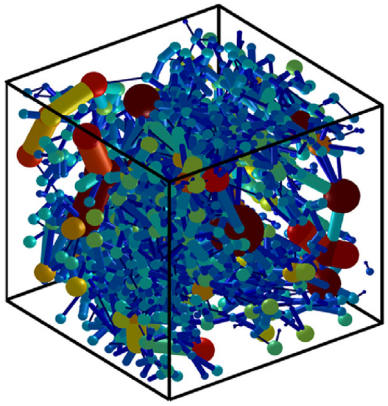

Fig. 3. PNM for OM.

Considering unsteady flow, according to the continuity equation of the compressible fluid, the mass of the gas in a single pore in the pore network satisfies:

$$\sum_j g_{ij}\left(p_j - p_i\right) = \frac{\partial(V_i\rho_i)}{\partial t} + \frac{\partial\left(q_\mu\right)}{\partial t} \tag{1}$$

where $g_{ij} = \frac{K_{app}\pi {r_{ij}}^2}{\mu l_{ij}}\rho_{avg}$ is the conductivity coefficient between pore i and j, p_i and p_j are the gas pressure of pore i and j, V_i and ρ_i are the pore volume and gas density in pore i, q_μ denotes the excess adsorbed gas (here, the excess adsorbed gas is used to avoid the overlap of free gas and adsorbed gas, which is different from the usually used total adsorbed gas), $\rho_{avg} = \frac{(p_i+p_j)M}{2ZR_{gas}T}$ is the gas density in the throat, K_{app} denotes the apparent permeability of the throat, r_{ij} and l_{ij} are the radius and length of the throat connecting the pores, R_{gas} is the universal gas constant. μ is the gas viscosity calculated by Lee's equation considering the real-gas effect [30], Z is the compressibility factor calculated by Dranchk-Abu-Kassem method [31].

Record the amount of free gas as $q_f = V_i\rho_i$, the equation can be abbreviated as:

$$\sum_j g_{ij}\left(p_j - p_i\right) = \frac{\partial q_f}{\partial t} + \frac{\partial q_\mu}{\partial t} \tag{2}$$

Considering viscous flow, slippage and diffusion, the apparent permeability of the throat is calculated by the Javadpour's equation [17]:

$$K_{app} = \frac{2r_{ij}}{3RT}\frac{\mu M}{\rho_{avg}}\sqrt{\frac{8R_{gas}T}{\pi M}} + \left[1 + \sqrt{\frac{8\pi R_{gas}T}{M}}\ \frac{\mu}{p_{avg}r_{ij}}\left(\frac{2}{\alpha} - 1\right)\right]\frac{{r_{ij}}^2}{8} \tag{3}$$

Eq. (2) is solved by a semi-implicit method, where the pore pressure on the left side of the equation is calculated by the value of $n+1$ time step, while the right side of the equation is calculated by the value of n time step. And the flow term coefficient g_{ij} is also calculated by an explicit method. Recording $C_\mu^n = \frac{1}{\Delta t}\left(\frac{\partial q_\mu}{\partial p}\right)^n$ and $C_f^n = \frac{1}{\Delta t}\left(\frac{\partial q_f}{\partial p}\right)^n$, Eq. (2) is further linearized as:

$$\sum_j {g_{ij}}^n\left(p_j^{n+1} - p_i^{n+1}\right) = \left(C_\mu^n + C_f^n\right)\left(p_i^{n+1} - p_i^n\right) \tag{4}$$

Let $\delta p = p^{n+1} - p^n$, we have:

$$\sum_j {g_{ij}}^n\left(p_j^n - p_i^n\right) + \sum_j {g_{ij}}^n\left(\delta p_j - \delta p_i\right) = \left(C_\mu^n + C_f^n\right)\delta p_i \tag{5}$$

δp is the unknown in the equation and is calculated by solving the above algebraic equations.

As the relatively large specific surface area of OM, the adsorbed gas in OM cannot be ignored. In this work, the amount of adsorbed gas is calculated as Jiang et al. [32]:

$$q_\mu = S_{surface,i} \cdot \left(\frac{V_L p}{p_L + p}\right)\left(1 - \frac{\rho_{free}}{\rho_{ad}}\right) \cdot \frac{16.06 \times 10^{-3} kg/mol}{22400 ml/mol} \tag{6}$$

where $S_{surface,i}$ is the surface area of pore i. When calculating the volume and surface area of the pores, half of that of the throats connected to the pores are also included to increase the accuracy. Without loss of generality, the pores are regarded as spheres and the throats are regarded as straight cylindrical pipes. In Eq. (6), q_μ is in kg, Langmuir volume V_L is in ml/m^2, Langmuir pressure p_L and gas pressure p are in Pa, adsorption phase density ρ_{ad} and free phase density ρ_{free} are in kg/m^3.

The parameters obtained by MD simulation is adopted in the calculation of excess adsorption capacity. MD calculation can cover the nano-scale adsorption characteristics, making the obtained parameters closer to physical reality (Appendix A). From the calculated isotherm adsorption curves, the three-parameter Langmuir equation, which is also named the modified Langmuir equation [33], is fitted and the relations between the three parameters with the temperature is given:

$$\begin{cases} V_L\left(mL/m^2\right) = -6.0 \times 10^{-4}T(K) + 0.41 \\ p_L(MPa) = 5.6 \times 10^{-2}T(K) - 13.67 \\ \rho_{ad}\left(g/cm^3\right) = -3.4 \times 10^{-4}T(K) + 0.42 \end{cases} \tag{7}$$

Using Eq. (6) and Eq. (7), the excess adsorption amount at different temperatures and pressures can be easily calculated. In gas release process, as the pore pressure drops, free gas phase and adsorbed gas phase are exchanging in OM, and then discharge into IOM through the boundary of the pore networks.

2.2. IOM

IOM is modeled by FVM. Considering the effects of natural fractures and hydraulic fractures, Darcy flow is used here. And the porosity and the permeability of IOM are regarded as homogeneous. Despite the distribution of fractures is heterogeneous for a real well, we hypothesize the heterogeneity can be ignored in a small local area of micrometer. A larger range of IOM permeability value (from nD to mD) is set to obtain results under different fracturing effects.

For the dynamic flow of compressible fluid, the combination of Darcy's law and the continuity equation (or the matter conservation equation) leads to:

$$\nabla \cdot \left(\frac{\rho K}{\mu}\nabla p\right) = \frac{\partial(\rho\varphi)}{\partial t} \tag{8}$$

Integrate the differential equation above in the control volume V, one gets:

$$\iint_{\partial\Omega}\left(\nabla\cdot\left(\frac{\rho K}{\mu_g}\nabla p\right)\right)d\vec{s}=\iiint_{\Omega}\left(\frac{\partial(\rho\varphi)}{\partial t}\right)dV \tag{9}$$

A cubic grid is used to discretize the integral equation. For grid i, we have:

$$\sum_j\frac{KA_{ij}}{\mu l_{ij}}\rho_{avg}\left(p_j-p_i\right)=\frac{\partial(V\rho\varphi)}{\partial t} \tag{10}$$

where $T_{ij}=\frac{K_sA_{ij}}{\mu l_{ij}}\rho_{avg}$ is the conductivity between grid i and j, $\rho_{avg}=\frac{(p_i+p_j)M}{2ZR_{gas}T}$ is the gas density, $q_f=V\rho\varphi$ is the amount of free gas. The definitions of the parameters are almost similar to the definition in the pore network in Section 2.1, so they are not be repeated here. The primary difference is that the control volume in PNM is the pore while in FVM is the porous medium; and the connecting channel in PNM is the throat while in FVM is the interface between the porous media.

Similar to Section 2.1, Eq. (10) can also be abbreviated as:

$$\sum_j T_{ij}\left(p_j-p_i\right)=\frac{\partial q_f}{\partial t} \tag{11}$$

The above equation is solved using a semi-implicit method. The grid pressure on the left side of the equation is calculated by the value of $n+1$ time step, and the cumulative term coefficient and the flow term coefficient are calculated by the value of n time step. Recording $C_f^n=\frac{1}{\Delta t}\left(\frac{\partial q_f}{\partial p}\right)^n$, Eq. (11) is further linearized as:

$$\sum_j {T_{ij}}^n\left(p_j^{n+1}-p_i^{n+1}\right)=C_f^n\left(p_i^{n+1}-p_i^n\right) \tag{12}$$

Let $\delta p=p^{n+1}-p^n$, we have:

$$\sum_j {T_{ij}}^n\left(p_j^n-p_i^n\right)+\sum_j {T_{ij}}^n\left(\delta p_j-\delta p_i\right)=C_f^n\delta p_i \tag{13}$$

δp is the unknown in the equation, which is calculated by solving the above algebraic equations.

2.3. Interface coupling

Mortar method is used to couple organic PNM and inorganic FVM, as shown in Fig. 4. Mortar method is a domain decomposition algorithm that combines finite element approximation and spectral element approximation. The advantages of Mortar are that it allows for different physics, scales, and models in various subdomains and is parallelizable. It would be of great value if the subdomains could be modeled through different methods which are appropriate to their local transport conditions and levels of accuracy. Balhoff et al. [34] used Mortar method to realize the coupling between pore network and finite element for the first time. The core ideas of Mortar method are: (1) Using the pressures of Mortar nodes and basis functions to obtain the boundary pressures of the subdomains to ensure the continuity of the interface pressure. (2) Iterating pressure to make the integrated flux of the subdomains on the left and right sides close to zero, which ensures the weak matching of the flux in the interface.

In the implicit dynamic calculation, the pressure field in the Mortar space (or in the interface) is unknown, which can be given by the basis functions $\varphi(x,y)$ and their coefficients α^{n+1} in $n+1$ time step:

$$p^{n+1}(x,y)=\sum_j {\alpha_j}^{n+1}\varphi_j(x,y) \tag{14}$$

In this work, the quadrilateral element and the piecewise continuous bi-linear basis functions are applied. In order to make the fluxes of the left and right subdomains adjacent to the interfaces are integrally conservative, one obtains:

$$\begin{aligned}F_j^{n+1}&=\sum_i^{N_L}\varphi_j(x_{Li},y_{Li}){q_{Li}}^{n+1}-\sum_i^{N_R}\varphi_j(x_{Ri},y_{Ri}){q_{Ri}}^{n+1}\\&=0,(j=1,2,\ldots,n_{Mortar})\end{aligned} \tag{15}$$

where (x_{Li},y_{Li}) and (x_{Ri},y_{Ri}) are the coordinates of the FVM nodes or PNM pores in the left and right side of the interface, N_L and N_R are the number of those nodes or pores, ${q_{Li}}^{n+1}$ and ${q_{Ri}}^{n+1}$ are the fluxes in the left and right side of the interfaces, respectively. n_{Mortar} = basis function number = Mortar node number.

The key to solving the problem is to find appropriate ${\alpha_j}^{n+1}$ so that $F_j^{n+1}=0$. The implicit dynamic coupled solution algorithm is given below:

1. Pressure field at n time step is known.
2. Give a conjecture of ${\alpha_j}^{n+1}$ at $n+1$ time step.
3. Assign values to the boundary pressures of the subdomains on both sides of Mortar space using $p^{n+1}(x,y)=\sum_j{\alpha_j}^{n+1}\varphi_j(x,y)$.
4. Calculate the pressure field at $n+1$ time step of the subdomains.
5. Based on the pressure field of the subdomains, calculate the flow of the pores or nodes in the interface, and then calculate the

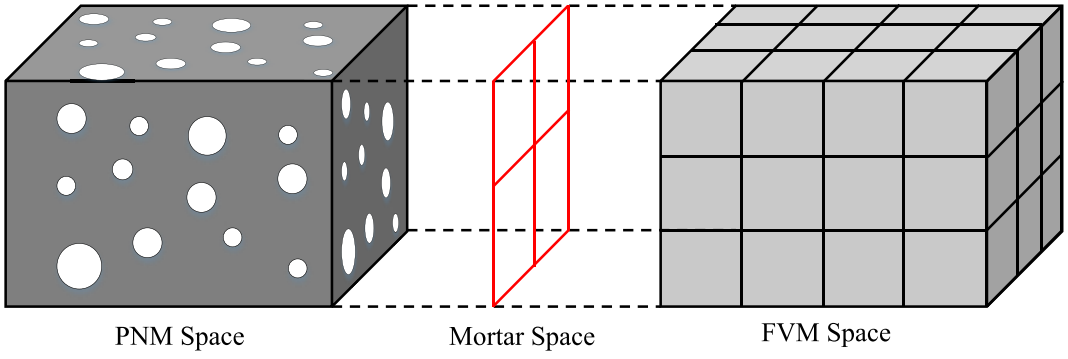

Fig. 4. Mortar coupling PNM and FVM.

integrated flow on the left and right sides of the Mortar space, F_j^{n+1}.

6. Construct the Jacobian matrix $J_{i,j} = \frac{\partial F_i}{\partial \alpha_j}$ and solve $[J]d\vec{\alpha} = -\vec{F}$, if the maximum value of $d\vec{\alpha}$ is less than the given error limit ε, the pressure field at $n+1$ time step is obtained, and then go to step 1; if $\max(d\vec{\alpha}) > \varepsilon$, then update α_j^{n+1} using $\alpha_j^{n+1} = \alpha_j^{n+1} + d\alpha_j$ and return to step 3.

3. Progress in time

According to the pressure field at the moment t, the interface mass-exchange-rate of OM and IOM can be calculated by the total flow rate on either side of the interface. For example, on the side of IOM, using nodes on the interface, the instantaneous mass-exchange-rate q_{ex} at the time t is calculated:

$$q_{ex} = \sum_{i \in Interface} \sum_{j} \frac{KA_{ij}}{\mu l_{ij}} \rho_{avg} \left(p_j - p_i\right) \tag{16}$$

In addition, according to the node pressure at the outer boundary, the production rate of the outer boundary, q_{out}, can be calculated as:

$$q_{out} = \sum_{i \in OuterB} \sum_{j} \frac{KA_{ij}}{\mu l_{ij}} \rho_{avg} \left(p_j - p_i\right) \tag{17}$$

Mortar method is easily parallel computing, because each subdomain can be solved separately in the process of solving the Jacobi matrix, and then gradually matched in the iterative process. For parallel design, one can refer to the work of Cao et al. [23].

4. Interface gas exchange of OM and IOM

4.1. Model comparison

In this section, MDCM is compared with a single medium model. In order to ensure the consistency of the parameters during the comparison, the static upscaled parameters corresponding to MDCM are used in the single medium model. This approach therefore offers a comparison between the usually used upscaling method for parameters with the upscaling for dynamic processes, hence provides insights into the microscale mechanism of tail production.

The single medium model uses FVM for modeling. In this model, OM and IOM are not separated and a global meshing is applied, as shown in Fig. 5a. The local heterogeneity between OM and IOM is homogenized. The parameters in each finite volume grid are upscaled from the parameters in MDCM to ensure their correspondence in the comparison. These parameters include permeability, porosity, and adsorption capacity. According to our previous research [23,24], based on the water-electricity similarity effect, using a series-parallel method, the permeability of the single medium model can be calculated by OM permeability K_{OM}, IOM permeability K_{IOM} and volumetric total organic carbon (TOC) ω:

$$K = \frac{K_{IOM}}{\omega^{1/3} K_{IOM} / \left(\omega^{2/3} K_{OM} + \left(1 - \omega^{2/3}\right) K_{OM}\right) + \left(1 - \omega^{1/3}\right)} \tag{18}$$

For porosity, the total pore space includes organic pores and inorganic pores:

$$\varphi = \varphi_{OM}\omega + \varphi_{IOM}(1 - \omega) \tag{19}$$

where ω is volumetric TOC, φ is porosity of shale, φ_{OM} is porosity of OM and φ_{IOM} is porosity of IOM. As for adsorbed gas, adsorption is only assigned in OM in MDCM, so when comes to the single medium model, the surface area of OM is used to represent that of shale and then homogenized to each grid.

Through the upscaling method for static parameters above, it is ensured that the single media model is consistent with MDCM in terms of total porosity, permeability, adsorption capacity, and thus gas content (includes adsorbed gas in OM and free gas in OM and IOM). The corresponding parameters are shown in Table 1.

With the parameters kept corresponding, the degassing process of the two models are simulated. Given the same initial pressure and boundary pressure (the initial pressure is set to 10 MPa and the outer boundary pressure is 1 MPa), the production process with constant outer pressure is calculated. Therefore, a simulation of gas recovery is conducted, which reduced the boundary pressure to 1 MPa and used reservoir pressure drive to produce gas at the boundary. The temperature is 350 K. After simulations, the gas production rates and the cumulative gas productions at different times of the two models are compared, as shown in Fig. 6 and Fig. 7.

Comparing the gas production rates of the single medium model and MDCM (Fig. 6), it is shown that MDCM has a lower production rate in the early stage while a much higher production rate later. The production rate in the later stage calculated by the two models can differ by 1–2 orders of magnitude. This is because the fast and slow processes of gas flow are accounted in MDCM, the slow process brings a much greater gas production potential in the later stage.

Fig. 7 illustrates the cumulative gas productions of the two models. Results show that the cumulative gas productions of the two models tend to be consistent after a long enough time. This phenomenon results from the same gas content in the two models, which also stands for a verification for MDCM. The interaction of the slow and fast transport mechanisms diminishes gas production in the short term, but compensates it in the long term.

The primary difference between the two models is their deflation duration, as shown in Fig. 7, the deflation duration of MDCM can reach about tenfold that of the single medium model. The results show that MDCM can capture this dynamic interaction of OM and IOM from the micro-scale. We demonstrate that the microscale dynamic process affects not only the production rate, but more importantly the lifetime of the shale gas well. This is the first time putting insight into the interface mass exchange between OM and IOM by microscale coupled simulation. The significant impact of the dynamic gas exchange between OM and IOM on tail production, previously captured through rock-scale simulation with a set of assumptions [9], is confirmed at the microscale. Governments and industry must recognize that shale gas is not a resource which quickly returns on investment but a resource for sustained long-

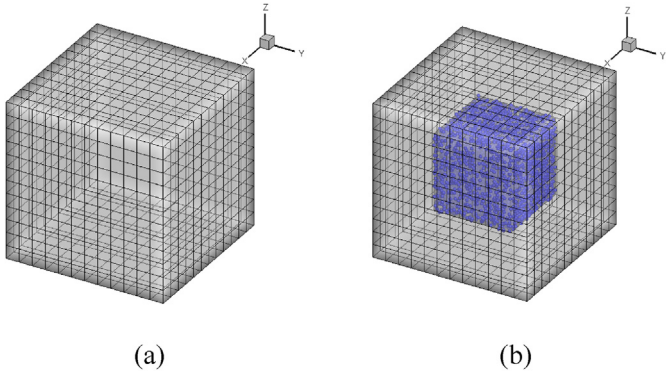

Fig. 5. Model comparison, (a) the single medium model (b) MDCM.

Table 1
Corresponding parameters of the single medium model and MDCM.

Parameters	The single medium model	MDCM	
		OM	IOM
Porosity (%)	0.029	0.160	0.010
Permeability (m^2)	8.74×10^{-17}	1.05×10^{-17}	1.00×10^{-16}
Adsorption surface area (m^2)	1.85×10^{-9}	1.85×10^{-9}	0

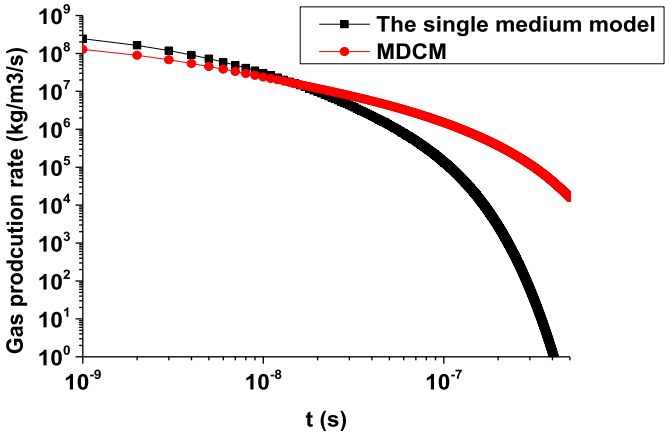

Fig. 6. Comparison of the gas production rates of the two models.

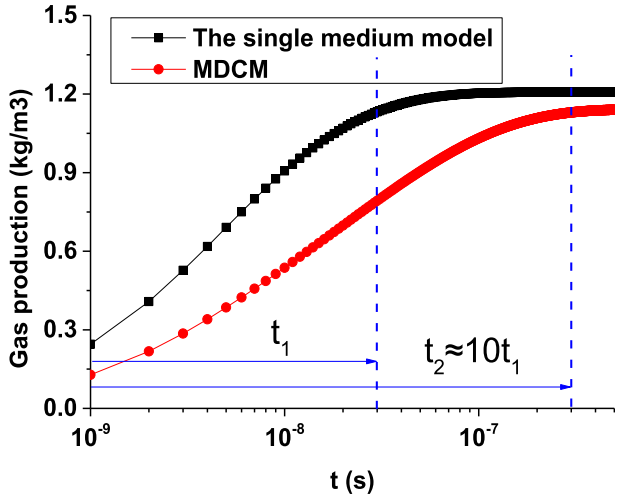

Fig. 7. Comparison of the cumulative gas productions of the two models.

term benefits. This observation has profound implications in the potential revitalization of the hundreds of thousands of shale gas wells around the world considering their long-time production properties.

4.2. Semi-analytical relations for interface gas exchange

The above research captures the dynamic interaction between OM and IOM. Following this, an in-depth analysis of the mass transfer mechanism between OM and IOM is necessary. A concise physical expression of the micro-scale phenomena is also important to establish a foundation for the macro-scale. Therefore, in this section, we derive a semi-analytical relationship for the interface mass-exchange-rate based on the essential characteristics of permeances and numerical simulations.

Firstly, we performed simulations under many working conditions and found that the entire production process has a two-stage behavior. Taking the initial pressure of 10Mpa and the boundary pressure of 5Mpa as an example, the variations of average internal gas pressures in OM and IOM and the mass-exchange-rate variations in production are shown in Fig. 8. We demonstrates that the pressure difference between OM and IOM has two regimes: it increases with time in Stage I and then decreases in Stage II. In Stage I, the pressure difference between the two subdomains increases because gas in IOM releases more rapidly than in OM. While in Stage II, gas in OM is also released and finally both the pressures of OM and IOM tend to be consistent with the boundary pressure. In addition, the variation of the mass-exchange-rate with t also has those two stages. In Stage I, the mass-exchange-rate rapidly increases, indicating that the interface exchange between OM and IOM rapidly accelerated; while in Stage II, the mass-exchange-rate turns to decrease with time. When the pressure difference tends to zero, the interface gas exchange will shut down.

Furthermore, the relationship between the mass-exchange-rate and the pressure difference is analyzed, as shown in Fig. 9. Interestingly, except for a short-term nonlinearity, the mass-exchange-rate depends linearly on the pressure difference for most of the time. There is a substantial difference in performance between short-term gas exchange and long-term gas exchange of OM and IOM. The non-linear relationship period corresponds to the aforementioned Stage I, while the linear relationship period corresponds

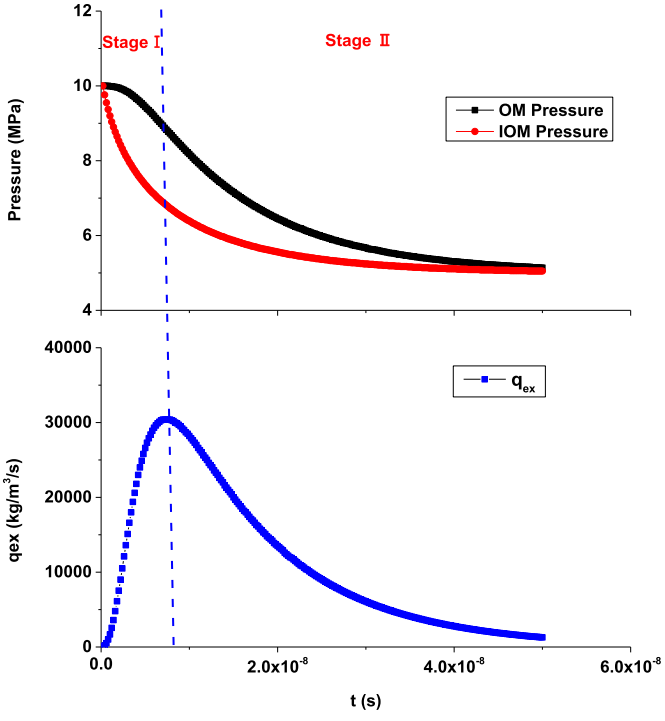

Fig. 8. The variations of gas pressures and the mass-exchange-rate with t.

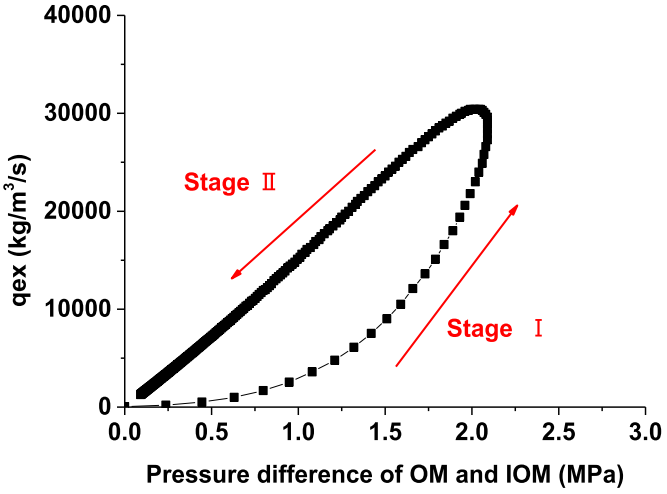

Fig. 9. The relationship between the mass-exchange-rate and pressure difference.

to Stage II. From a long-term perspective, Stage II dominates the production with a linear relationship between the mass-exchange-rate with the pressure difference. The linear stage occupies most of the production time thus more critical for the tail production of shale gas. In addition, it is interesting to note that this linear relationship is independent with the absolute pressure and time. These physical pictures are expected to deeply impact the dynamics at large scales.

To apprehend the detailed exchange process, we extended our investigation using theoretical analyses. According to the basic characteristics of permeance, similar to Darcy's flow, the mass-exchange-rate should be related to permeability, gas density, gas viscosity, interface area, and the characteristic length. The linear relationship in Stage II is accordingly in the form:

$$q_{ex} \propto \frac{K}{\mu}\frac{S}{L}\rho(p_{OM} - p_{IOM}) \tag{20}$$

where q_{ex} is mass-exchange-rate, kg/(m^3·s); ρ and μ are the gas density in kg/m^3 and gas viscosity in Pa·s; p_{OM} and p_{IOM} are the average internal gas pressures in OM and IOM respectively, Pa, V is the volume of the model, m^3, S is the interface area, L is the characteristic length of the seepage (here, is the side length of the shale block, 10 μm in this work).

The permeability in the formula should be the permeability in the interface, considering the permeability of organic matter and inorganic matter are unequal, it is expressed as the harmonic mean of the permeability of OM and IOM:

$$K_c = \frac{2K_{OM}K_{IOM}}{K_{OM} + K_{IOM}} \tag{21}$$

Further, according to the dimension of q_{ex}, the relationship of the q_{ex} is given as:

$$q_{ex} = \overline{q}_{ex}\frac{S}{V}\frac{1}{L}\frac{K_c\rho}{\mu}(p_{OM} - p_{IOM}) \tag{22}$$

where $\overline{q}_{ex}$ is the dimensionless mass-exchange-rate. OM is assigned to located in the center of the shale block, despite its simplicity, previous studies [24] has shown that the spatial distribution of OM has a limited impact on gas seepage. Therefore, according to the local volume content of OM ω (local volumetric TOC) and the length of the block, the interface area can be calculated as:

$$S = \left(L\sqrt[3]{\omega}\right)^2 \tag{23}$$

And $V = L^3$, so Eq. (22) can be further simplified as:

$$q_{ex} = \overline{q}_{ex}\frac{\left(\sqrt[3]{\omega}\right)^2}{L^2}K_c\frac{\rho}{\mu}(p_{OM} - p_{IOM}) \tag{24}$$

It can be seen that the above formula covers the main factors that affect mass-exchange-rate: OM-IOM pressure difference, TOC, characteristic length of the shale block, permeability, gas density and viscosity. The remaining dimensionless mass-exchange-rate coefficient, $\overline{q}_{ex}$, reflects the difficulty of the interface exchange between OM and IOM, which will be analyzed in details below.

4.3. Dimensionless mass-exchange-rate coefficient $\overline{q}_{ex}$

4.3.1. Calculating the coefficient from numerical results

In order to obtain the dimensionless mass-exchange-rate coefficient $\overline{q}_{ex}$, MDCM simulation is used to obtain the curve of the mass-exchange-rate to the pressure difference of OM and IOM at first, then linear fitting is performed on Stage II to obtain the slope k, and finally $\overline{q}_{ex}$ is calculated using Eq. (24). Taking the IOM permeability of 1000 nD, TOC of 3, temperature of 350 K, and the average organic pore radius of 10 nm, 20 nm, and 30 nm as examples, the calculation process is introduced. The pore radius distribution, the throat radius distribution and the coordination number distribution of OM all obey the lognormal distribution. The standard deviations of the three distributions are set to 0.25. The average throat radius is set to 0.7 times the average pore radius, and the average coordination number is set to 6. According to these distributions, a random pore network for OM is constructed and then coupled with IOM. Different OMs are generated using the average organic pore radius of 10 nm, 20 nm, and 30 nm. Fig. 10 illustrates the pore structures and the pore sizes in the three cases. Then the curves of the mass-exchange-rate to the pressure difference of OM and IOM are calculated by MDCM, and the Stage II of the curves are linear fitted, as shown in Fig. 11.

Fig. 11 shows that all the curves under different working conditions are with two regimes, the non-linear Stage I ends quickly (the time interval between the points in the figure is the same, the little number of the points in Stage I indicts its short time), while the linear Stage II lasts a long time. After the simulation, the linear fitting is applied to Stage II. The slopes of the linear fitting curves are thus obtained, and their R-squared are above 0.99. According to the semi-analytical formula derived in Section 3.2 and the numerical calculations, the dimensionless coefficients are obtained, as shown in Table 2.

4.3.2. Parameter influence

In this section, the influence of parameters on the dimensionless mass-exchange-rate coefficient $\overline{q}_{ex}$ is investigated. At first, we found that the permeability ratio of OM and IOM has a great influence on $\overline{q}_{ex}$. Therefore, a series of permeability ratios are also included in the analysis of the influence of various parameters.

(1) Influence of parameters of OM. The influence of the average value and the standard deviation of organic pore radius on $\overline{q}_{ex}$ are shown in Fig. 12 and Fig. 13. Results show that the average organic pore radius has a great influence, while the standard deviation has little influence. For the permeability ratio less than 0.01, $\overline{q}_{ex}$ decreases as average organic pore radius increases. Inversely, for the permeability ratio greater than 0.01, $\overline{q}_{ex}$ increases as average organic pore radius

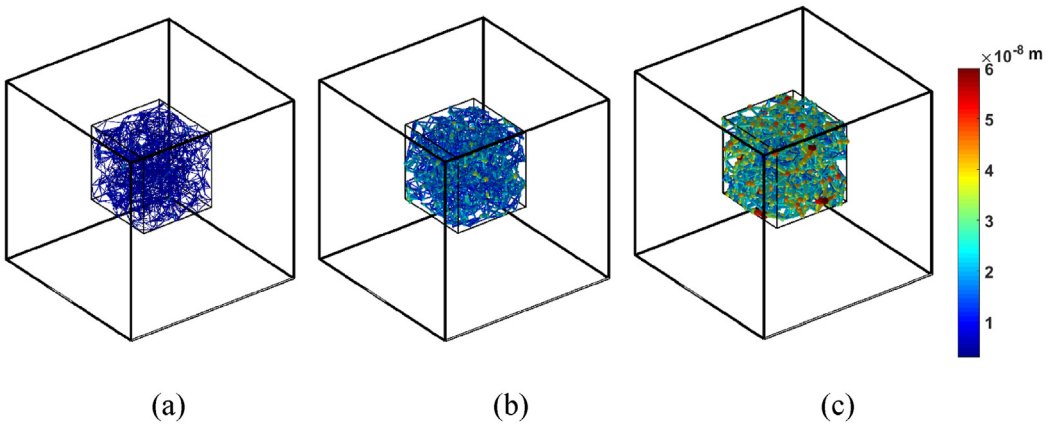

Fig. 10. Cases with different average organic pore radius, R_{OM}: (a) 10 nm, (b) 20 nm, (c) 30 nm.

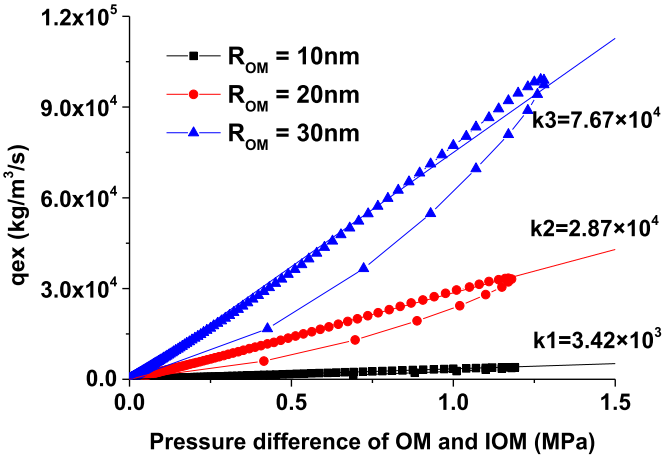

Fig. 11. Linear fitting of the Stage II.

increases. The average organic pore radius affects not only the permeability of OM, but also the porosity of OM. With other parameters remain certain, the pore size of OM has a great influence on its gas flow and storage, and thus has a great influence on the interface mass exchange. With the increase of average organic pore radius, the permeability of OM increases, and the permeability ratio of OM to IOM also increases. The standard deviation of the pore radius of OM primarily affects the dispersion degree of the pore size distribution, and has a weaker effect on $\overline{q}_{ex}$ compared to the average pore size.

(2) Influence of parameters of IOM. The influence of inorganic porosity on $\overline{q}_{ex}$ is further analyzed, with the parameters in OM remain unchanged, as shown in Fig. 14. Results show that inorganic porosity also has a significant influence on $\overline{q}_{ex}$. The influence of inorganic porosity on $\overline{q}_{ex}$ is slightly weaker only when the permeability of OM is much lower than that of IOM. The closer the organic permeability and inorganic permeability, the greater the influence of inorganic porosity on $\overline{q}_{ex}$. When the permeability ratio of OM and IOM is between 0.01 and 1, there is a multiple relationship between $\overline{q}_{ex}$ and the inorganic porosity.

(3) Influence of the relative proportion of OM and IOM in shale. Different TOC cases are established, with the porosity and permeability of the random pore network standing for OM kept close. The effective porosities of OMs are about 1% and the permeabilities are about 90nD. Under different TOC cases, the variation of $\overline{q}_{ex}$ to permeability ratio is obtained, as shown in Fig. 15. Fig. 15 suggests that TOC has a limited effect on the dimensionless coefficient. In fact, since the volumetric TOC has been considered as one of the parameters in the semi-analytical relation as Eq. (24), so its influence on the slope of the linear stage is covered. Thus, TOC has a weak influence on the dimensionless coefficient.

(4) The influence of temperature. A wide temperature range is set in the analysis, from 300 K to 400 K, as shown in Fig. 16. We demonstrate that temperature has negligible effect on the dimensionless coefficient. In this study, the effect of temperature is primarily on gas viscosity, and the effect of viscosity has also been covered in the semi-analytical relationship in Eq. (24), so that temperature also has a limited effect on $\overline{q}_{ex}$.

4.3.3. Dimensionless relational expression

Through the analysis of the influence of the parameters above, it is found that the permeabilities and the porosities of OM and IOM have a significant impact on the dimensionless coefficient $\overline{q}_{ex}$. Despite the intrinsic complexity of such heterogeneous, multiscale porous media, $\overline{q}_{ex}$ is primarily controlled by two dimensionless parameters: the permeability ratio and porosity ratio of OM and IOM. Therefore, in this section, the results of a series of different parameters in Section 3.3.2 are summarized to obtain a relational

Table 2
The calculated dimensionless coefficients.

K_{IOM} (nD)	R_{OM} (nm)	K_{OM} (nD)	φ_{OM}	φ_{IOM}	Slope k kg/(m^3·s·Mpa)	$\overline{q}_{ex}$
1000	10	5.28	0.26%	0.1%	3.42×10^3	129.86
	20	90.25	1.02%	0.1%	2.87×10^4	69.07
	30	494.09	2.28%	0.1%	7.67×10^4	46.29

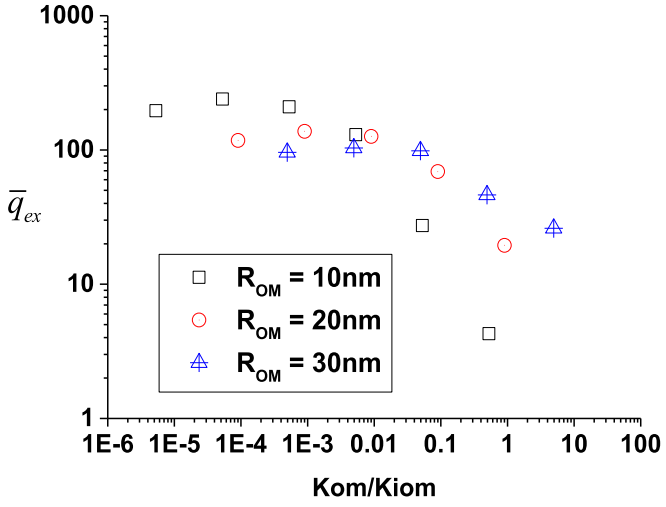

Fig. 12. Influence of average organic pore radius.

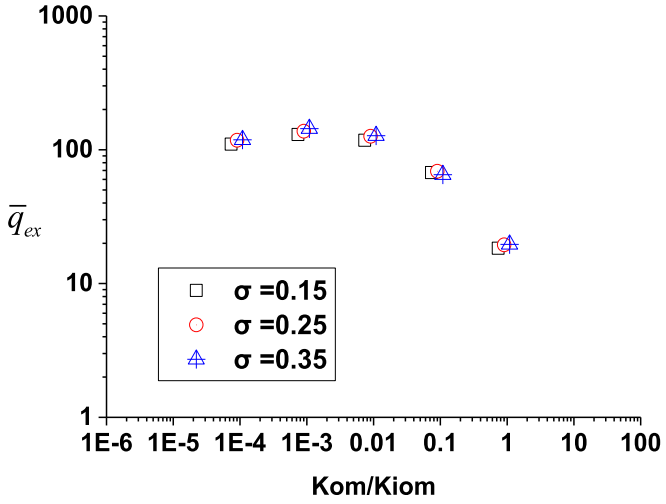

Fig. 13. Influence of the standard deviation, σ of the organic pore radius distribution.

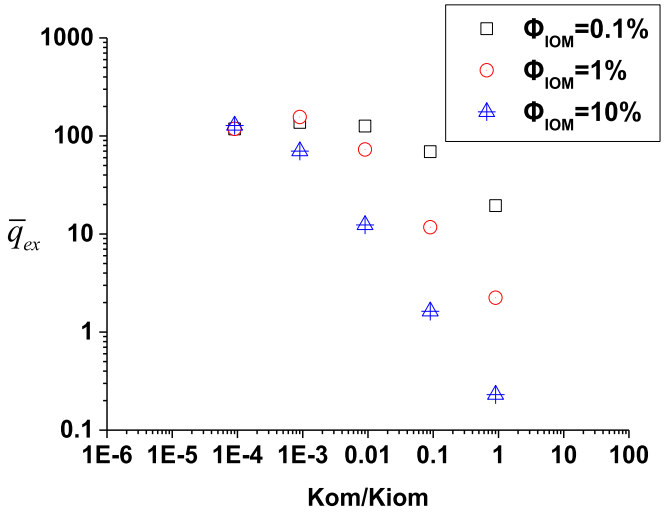

Fig. 14. Influence of the porosity of IOM.

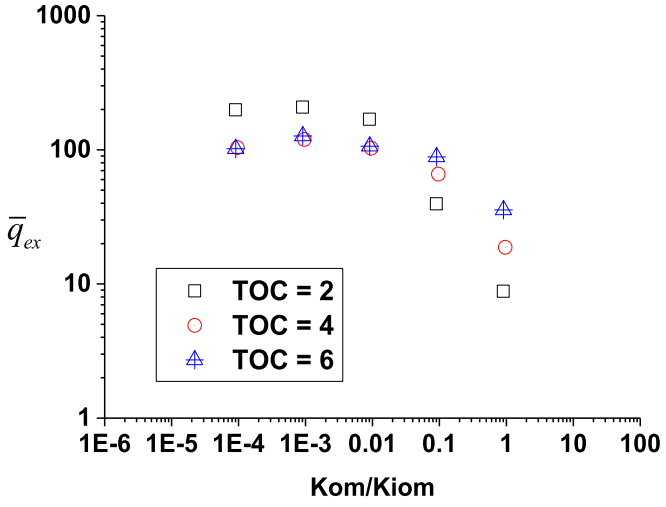

Fig. 15. Influence of TOC.

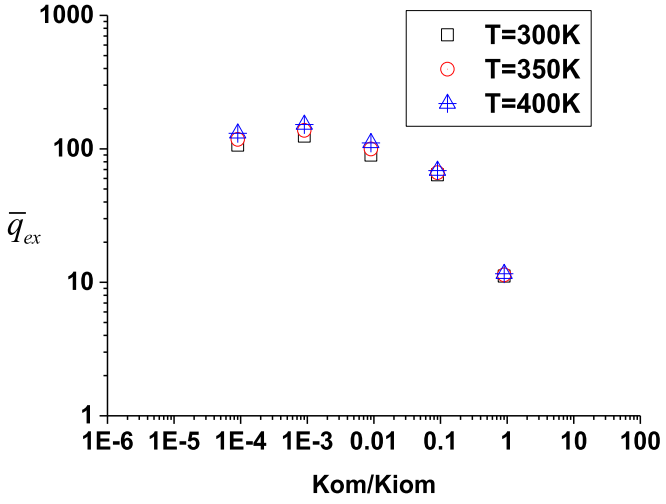

Fig. 16. Influence of temperature.

expression between the dimensionless parameters.

The calculation results of the aforementioned large number of calculation cases are put into a three-dimensional graph (scattered points in Fig. 17), in which the permeability ratio and the porosity ratio of OM and IOM are used as independent variables. The influence of the average organic pore radius, the standard deviation of the distributions, and the porosity of IOM are therefore covered in the two independent dimensionless parameters.

Furthermore, a practical dimensionless expression is derived by fitting the three-dimensional scatters.

(1) Viewed from a global perspective, the calculation result is similar to a quadric surface. A quadric surface is used to fit the global calculated cases, as shown in the blue surface in Fig. 17a. The permeability ratio is secondarily fitted, the porosity ratio is linearly fitted, with the R-squared (R^2) of 0.96. The dimensionless expression obtained is as follows:

$$\begin{aligned} \lg\overline{q}_{ex} &= 0.194 - 0.943x + 0.996y - 0.110x^2 + 0.278xy, \\ & x\in(-6,0), R^2 = 0.96 \end{aligned} \tag{25}$$

where $x = \lg\frac{K_{OM}}{K_{IOM}}; y = \lg\frac{\varphi_{OM}}{\varphi_{IOM}}$.

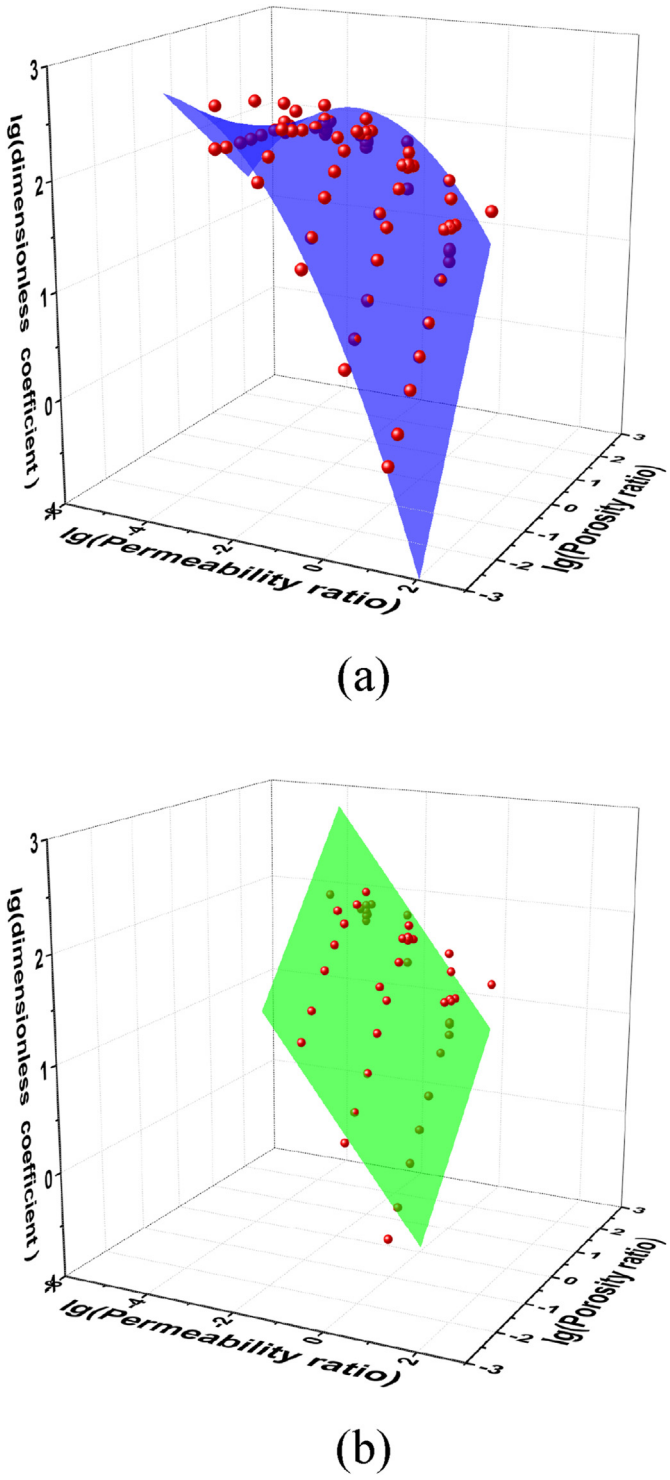

Fig. 17. Scatter graph of the dimensionless parameters and the fitted surface: (a) global quadric surface fitting, (b) local plane fitting.

(2) When the permeability ratio is greater than 10^{-3}, the calculated scattered points can be approximated by a three-dimensional plane to get a simple expression. So a bi-linear plane is used to fit the scatters with the permeability ratio greater than 10^{-3}, with the R^2 of 0.90, as shown in the green surface in Fig. 17b. And the local dimensionless relational expression is:

$$\lg\bar{q}_{ex} = 0.412 - 0.546x + 0.701y\ , x\in(-3,0)\ , R^2 = 0.90 \quad (26)$$

Furthermore, combining Eq. (24) with Eq. (25) and Eq. (26), the expressions for calculating the interface mass-exchange-rate of OM and IOM are also obtained. We emphasize that the relations are in no way imposed, but a result of the simulations and theoretical analyses.

For the permeability ratio ranging from 10^{-6} to 1, the interface mass-exchange-rate can be calculated as:

$$\begin{cases} q_{ex} = \bar{q}_{ex}\dfrac{\left(\sqrt[3]{\omega}\right)^2}{L^2}K_c\dfrac{\rho}{\mu}(p_{OM} - p_{IOM}) \\ \lg\bar{q}_{ex} = 0.194 - 0.943x + 0.996y - 0.110x^2 + 0.278xy, x\in(-6,0) \\ x = \lg\dfrac{K_{OM}}{K_{IOM}}; y = \lg\dfrac{\varphi_{OM}}{\varphi_{IOM}} \end{cases} \quad (27)$$

For the permeability ratio ranging from 10^{-3} to 1, a simplified relational expression for calculating the interface mass-exchange-rate can be used:

$$\begin{cases} q_{ex} = \bar{q}_{ex}\dfrac{\left(\sqrt[3]{\omega}\right)^2}{L^2}K_c\dfrac{\rho}{\mu}(p_{OM} - p_{IOM}) \\ \lg\bar{q}_{ex} = 0.412 - 0.546x + 0.701y, x\in(-3,0) \\ x = \lg\dfrac{K_{OM}}{K_{IOM}}; y = \lg\dfrac{\varphi_{OM}}{\varphi_{IOM}} \end{cases} \quad (28)$$

Through the expression above, the interface mass-exchange-rate can be efficiently and precisely calculated based on the relevant parameters in larger-scale models. In a dynamic process, the interface mass-exchange-rate can dynamically change with the pressures in OM and IOM, so that the microscopic behavior can be included in the macroscopic calculation. The relation offers a valuable tool for the gas transport properties in fractured shale.

4.4. Error analysis

In this section, an experiment of a real sample is introduced to analyze the error of the proposed relation. The sample comes from the Longmaxi Formation in Sichuan Basin, China. Longmaxi shale Formation is the main marine shale gas reservoir in China, which has been developed at commercial level and has huge resource potential. A relatively homogeneous shale sample is chosen in order to directly use the microscale result.

4.4.1. Experiments

The experiment process is shown in Fig. 18. Firstly, the pressure decay is measured by injecting helium gas (He) into particle sample using a system which consists of a reference cell, a sample cell, a series of values and high-precision transducers. High pressure gas gradually expands into the void volume in the crushed shale after gas expansion begins, which can be utilized to determine gas permeability and porosity by method reported by the American Gas Research Institute (GRI) [35]. The parameters in the experiment are listed in Table 3. Then, scanning electron microscope (SEM) imaging with the size of 400 × 400 μm^2 and the highest resolution of 4 nm is conducted on a field emission scanning electron microscope using a Zeiss-Merlin machine. Finally, through the three-dimensional reconstruction and pore network extraction, the organic PNM is obtained.

To calculate the smallest RES in the SEM image, four subdomains

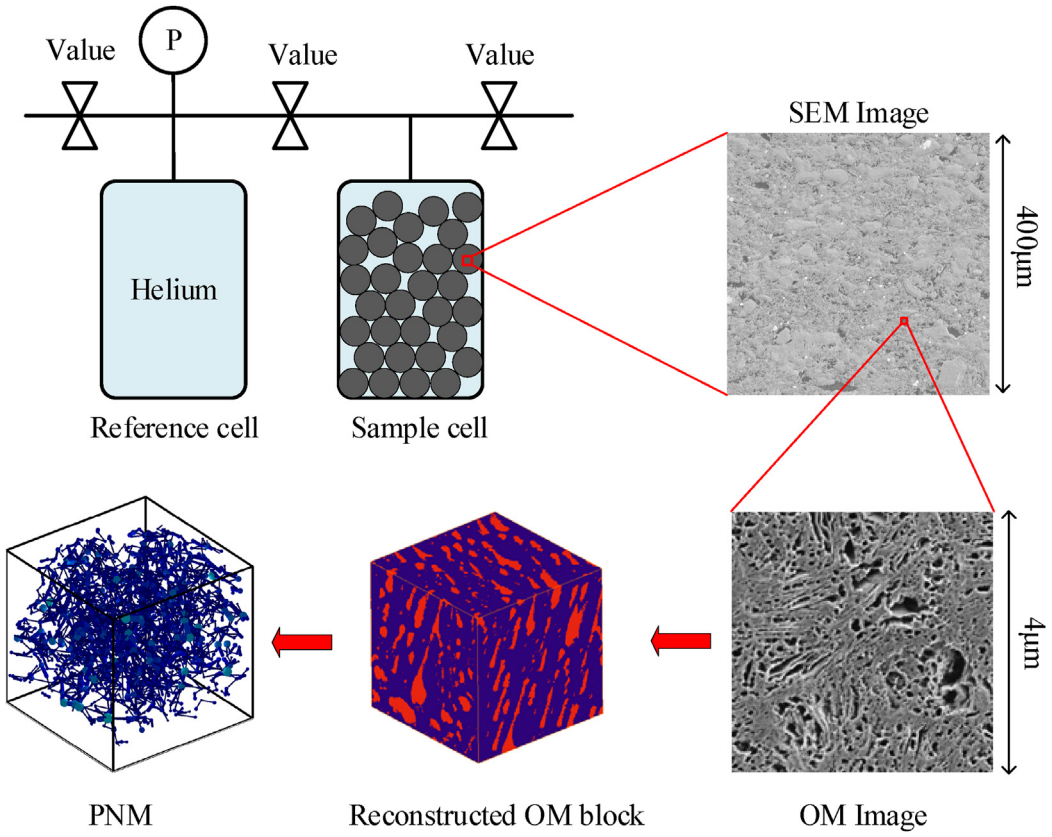

Fig. 18. Gas expansion experiment and SEM imaging.

Table 3
Parameters of the gas expansion experiment.

Parameter	Value
Particle radius (mm)	0.8
Sample mass (g)	57.62
Total volume of sample and reference cells (ml)	53.73
Initial pressure within sample particles (bar)	0.20
Initial pressure within the void volume of cells (bar)	7.77
Sample bulk density, (g/cm^3)	2.39
Temperature (K)	306
Sample porosity	9.51%
Gas type	Helium, 4 g/mol

of the SEM image are chosen, as shown in Fig. 19. The average grayscales in the subdomains reach a platform at about 200×200 μm^2, which shows a relatively homogeneous microscale structure. From the SEM image, the OM content is also calculated with the value of 9.83%. The organic pore types in the SEM are similar, so a typical OM image is chosen to reconstruct a 3D OM block using cross correlation based simulation-three step sampling (CCSIM-TSS) method [36]. From the reconstructed OM block, AB (axis & ball) algorithm [15] is applied to extract the pore network. From the pore network, OM permeability is calculated by Jiang's equation [6]. The effective porosity of the OM is 11%. And the parameters for calculating the permeability in three different directions are listed in Table 4. Table 4 shows that the OM block also has a relatively homogeneous pore structure, with weak anisotropy, and thus it can be represented by an isotropy porous media.

$R_{nt} = \left(\frac{1}{N}\sum_{i=1}^{N}\left(\frac{1}{r_i}\right)^{D_f-3}\right)^{-\frac{1}{D_f-3}}$ and $R_{avg} = \left(\frac{1}{N}\sum_{i=1}^{N}\frac{1}{r_i}\right)^{-1}$ are the average throat radius, N is the number of the throats, r_i is the radius of throat i. Φ_f is the flowing porosity. τ is the tortuosity. D_f is the surface fractal dimension. $K_{D,OM}$ is the intrinsic permeability of the OM.

4.4.2. Simulations and error analysis

After the experiments, a simulation is performed. After a trial calculation, the permeability ratio of OM and IOM is between 10^3 and 1, so the bi-linear relational expression, Eq. (28), is used. Shale sample is modeled by a symmetric regular sphere which has dual porosity. Gas confined in OM is used as a source term in the IOM equation. A homogeneous shale sample is chosen, so that the microscale gas exchange calculated in this work can be adopted without considering core-scale heterogeneities. The radius of particle samples is 0.8 mm, and the gas type is helium. Initial pore pressure is 0.20 bar and the initial boundary pressure is 7.77 bar. The total boundary volume is 53.73 ml, as there are plenty of particles, the total boundary volume is averaged. The porosity of IOM is calculated by the measured total porosity and the porosity of OM from SEM images. FVM modeling is used, and radial grids are

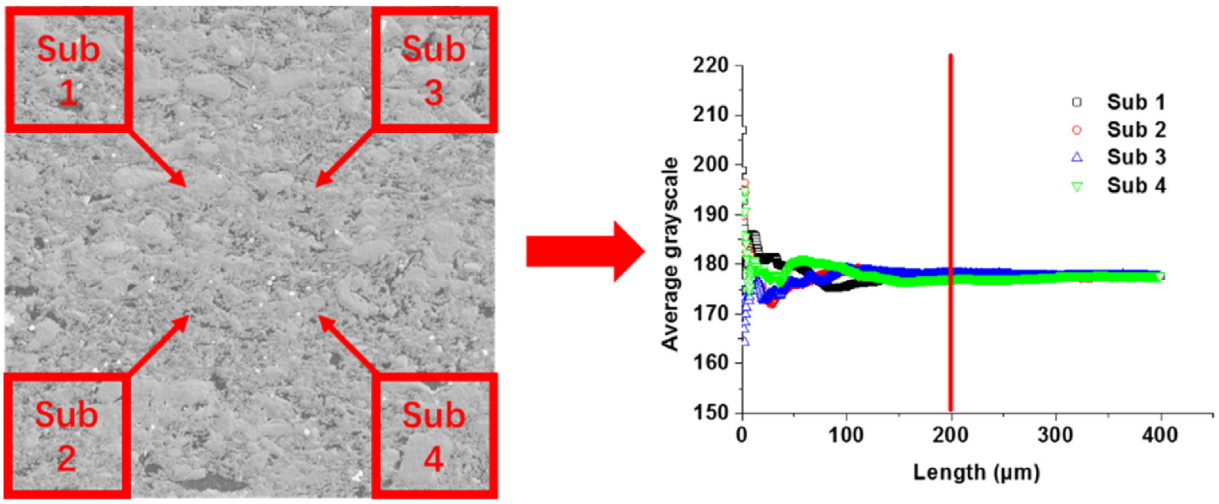

Fig. 19. RES calculation for the SEM image.

Table 4
Parameters of the OM.

Direction	R_{nt} (nm)	R_{avg} (nm)	Φ_f	T	D_f	$K_{D,OM}$ (nD)
X	3.98	3.69	0.003	2.92	2.67	13.32
Y	3.97	3.67	0.003	2.30	2.67	15.16
Z	3.99	3.69	0.003	1.96	2.67	14.67

adopted with the size of 10 μm. The governing equations are:

$$\begin{cases} \sum_j \dfrac{K_{IOM}A_{ij}}{\mu l_{ij}}\rho_{ij}\left(p_{IOM,j}-p_{IOM,i}\right)+q_{ex}V_i=\dfrac{\partial(V_i(1-\omega)\rho_i\varphi_{IOM})}{\partial t} \\ -q_{ex}=\dfrac{\partial}{\partial t}\left(\dfrac{p_{OM}M}{ZR_{gas}T}\omega\varphi_{OM}\right) \\ q_{ex}=\overline{q}_{ex}\dfrac{\left(\sqrt{3\omega}\right)^2}{L^2}\dfrac{2K_{OM}K_{IOM}}{K_{OM}+K_{IOM}}\dfrac{\rho}{\mu}(p_{OM}-p_{IOM}) \end{cases} \tag{29}$$

where K_{IOM}, φ_{IOM} and p_{IOM} are permeability, porosity and gas pressure of IOM; K_{OM}, φ_{OM} and p_{OM} are permeability, porosity and gas pressure of OM. q_{ex} is mass-exchange-rate coefficient and $\overline{q}_{ex}$ is its dimensionless value. Gas adsorption is ignored as the experimental gas is helium. K_{IOM} is the only parameter which needs to be determined by optimization with trial calculations. The unknowns in solving the equations are the pressures, p_{IOM} and p_{OM}. The equations are also solved using a semi-implicit time scheme. After the discretization and linearization, a solution can be easily obtained.

The pressure decay curves measured and simulated are shown in Fig. 20. K_{IOM} is 300nD. Fig. 20 shows that our method has smaller error with the experiment compared to the GRI method. This can be attributed to whether or not to include the interaction of the fast and the slow transports. The decay curve of the shale sample has obvious staging characteristics, which is different from a relatively

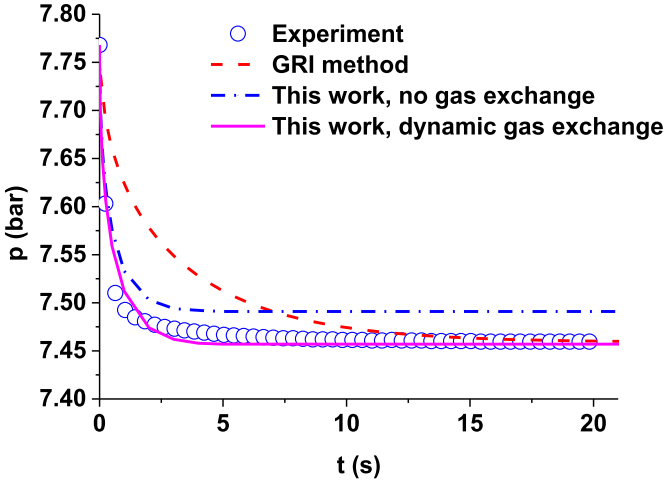

Fig. 20. Pressure delay curves measured and simulated.

uniform rock, such as sandstones. The late-time technique used in GRI method fits the later stage, thus it only contains the slow process and is hardly to access the fast process. The obtained experimental results demonstrate that our proposed model for shale gas transport can capture the long-term properties and that better performance can be obtained in terms of accuracy and precision than the current model. The advantage of GRI method is that it needs less information about the microscale OM properties, but this negligence will cause big error as to shale. This is because the short-term flow is controlled by IOM while the long-term flow is determined by OM, and the difference between the two subdomains should be carefully considered for shale gas. In addition, if the slow process in OM is ignored, large errors appear in the later stage. This result implicates that the dynamic gas exchange between OM and IOM is important for shale and needs to be considered. Prediction using our method is found to be in good

qualitative and quantitative agreement with experiment. The proposed dimensionless relation for calculating interface mass-exchange-rate is thus validated. Rigorous validation of this prediction against field-scale data requires more work, including experimental investigation on fractured systems. Nevertheless, despite the intrinsic complexity of the multi-scale transport, we provide a practical and efficient way for larger-scale simulations.

5. Conclusions

Reliable predictions of gas extraction from shale reservoirs are missing because conventional tools fail to account for their multi-scale complexity. In this study, we put insight into the detailed interface interaction between OM and IOM and give a microscale explanation of tail production. The deflation duration of MDCM can reach about tenfold that of the single medium model as the interaction of the fast and slow processes in shale gas flow is captured. Interestingly, we also discover a two-stage process in the variation of the mass-exchange-rate with the pressure difference of OM and IOM: it is nonlinear in Stage I and then turns to be linear in Stage II. Furthermore, through theoretical analysis, dimensional analysis and numerical simulations, an efficient and practical dimensionless relation for calculating interface gas exchange is obtained. The relation between the dimensionless parameters is obtained through the fitting of a large number of simulations with $R^2 \geq 0.90$. Finally, the accuracy and reliability of this relation are examined based on gas expansion experiment results. Better performance can be obtained in terms of accuracy and precision than the current model, as the difference between the subdomains in shale (OM and IOM) is carefully considered in our method. These results emphasize a change of paradigm from statistic to dynamic *trans*-scale transport. Governments and industry must recognize that shale gas is not a resource which quickly returns on investment but a resource for sustained long-term benefits. The herein constructed method can be readily used for predictions of tail production in multiscale approaches accounting for organic/inorganic interfaces, nanopore geometries and fracture networks. Further work is needed to fully characterize the distribution of fractures in gas shales, experimentally investigate on fractured systems and upscale the dynamic process to large-scales. This further improves the link between microscale constitutive models of porous materials and their engineering applications.

CRediT authorship contribution statement

Gaohui Cao: Conceptualization, Methodology, Investigation, Writing - original draft. **Wenbin Jiang:** Methodology, Writing - review & editing. **Mian Lin:** Methodology, Supervision. **Lili Ji:** Investigation. **Zhipeng Xu:** Investigation. **Siping Zheng:** Investigation. **Fang Hao:** Conceptualization, Methodology.

Declaration of competing interest

The authors declare that they have no known competing financial interests or personal relationships that could have appeared to influence the work reported in this paper.

Acknowledgement

This work was supported by the National Natural Science Foundation of China (Grant No. 42030808), the National Natural Science Foundation of China (Grant No. 41690132), the Strategic Priority Research Program of the Chinese Academy of Sciences (Grant No. XDA14010304), and the National Natural Science Foundation of China (Grant No. 41872163).

Appendix A. Molecular dynamics simulation for gas adsorption parameters

The basic idea of molecular dynamics (MD) simulation is to solve the Newtonian equation of motion of particles and obtain the dynamic values of the trajectory coordinates and speed of all particles in the system. A graphite channel, representing organic pores in shale, consists of upper and lower three-layer-graphite walls and a central void space. In the channel, adsorption is controlled by the van der Waals forces of methane-methane and methane-graphite. In this study, we adopt LAMMPS (Plimpton, 1995), an open-source MD software, and use the following Lennard-Jones potential function:

$$U(r) = 4\varepsilon\left[\left(\frac{\sigma}{r}\right)^{12} - \left(\frac{\sigma}{r}\right)^{6}\right] \tag{A.1}$$

where ε and σ represent the force field parameters and r denotes the distance of the molecule pair.

The excess adsorption per unit surface area was obtained by MD numerical simulation for a 3.8 nm graphite plate slit. Then the modified Langmuir equation [33] is used to fit the excess isotherms to get the three unknown parameters (V_L, p_L and ρ_{ad}):

$$q_{\mu,usurf} = \left(\frac{V_L p}{p_L + p}\right)\left(1 - \frac{\rho_{free}}{\rho_{ad}}\right) \tag{A.2}$$

where $q_{\mu,usurf}$ is the excess adsorption per unit surface area (ml/m^2).

Using MD simulation, the adsorption isotherms at different temperatures are calculated, as shown in Fig. A1.

From Fig. A1, the three adsorption parameters were calculated and then the relationship between the three parameters and the temperature was obtained, as shown in Fig. A2.

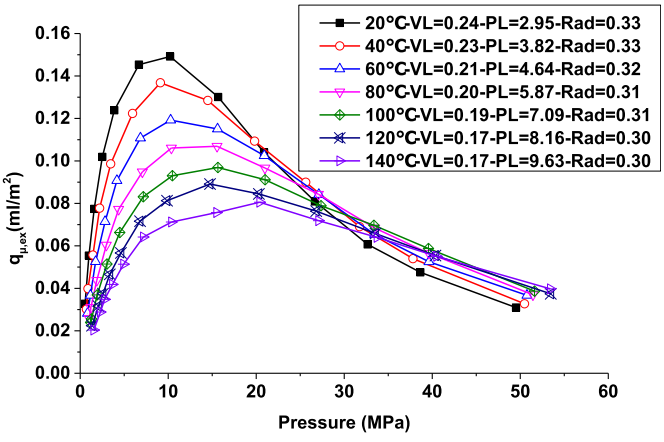

Fig. A.1. The adsorption isotherms at different temperatures.

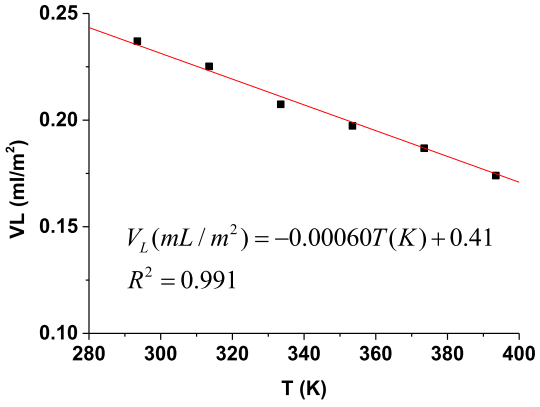

(a)

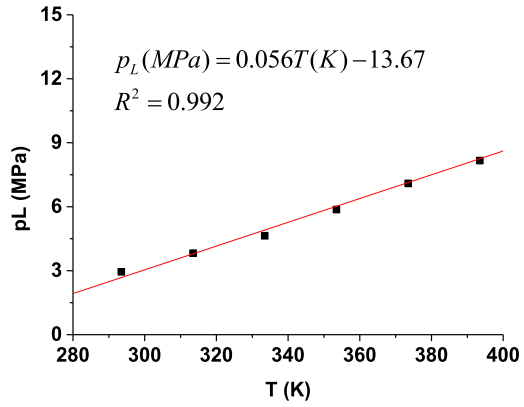

(b)

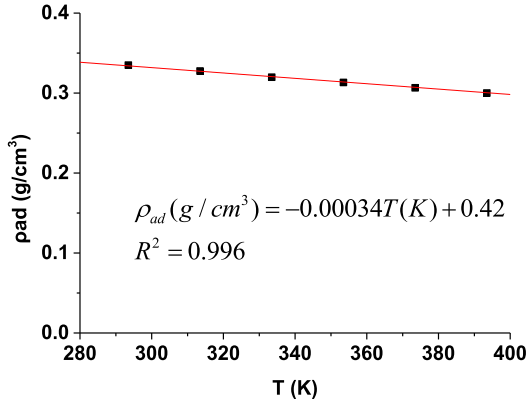

(c)

Fig. A.2. Fitting for the adsorption parameters (a) Langmuir volume, (b) Langmuir pressure, (c) adsorption phase density.

Through Fig. A2, the adsorption parameters can be simply calculated by the temperature. Combined with Eq. (A.2), the excess adsorption of per unit surface area in OM under different pressures and temperatures can be calculated using the following formula:

$$\begin{cases} q_{\mu,usurf} = \left(\dfrac{V_L p}{p_L + p}\right)\left(1 - \dfrac{\rho_{free}}{\rho_{ad}}\right) \\ V_L\left(mL/m^2\right) = -6.0 \times 10^{-4}T(K) + 0.41 \\ p_L(MPa) = 5.6 \times 10^{-2}T(K) - 13.67 \\ \rho_{ad}\left(g/cm^3\right) = -3.4 \times 10^{-4}T(K) + 0.42 \end{cases} \tag{A.3}$$

References

[1] Aydin G. Forecasting natural gas production using various regression models. Petrol Sci Technol 2015;33:1486–92.
[2] Aydin G. The modeling and projection of primary energy consumption by the sources. Energy Sources B Energy Econ Plann 2015;10:67–74.
[3] Kober T, Schiffer HW, Densing M, Panos E. Global energy perspectives to 2060 – WEC's world energy scenarios 2019. Energy Strat Rev 2020;31:100523.
[4] Bilgili F, Koçak E, Bulut Ü, Sualp MN. How did the US economy react to shale gas production revolution? An advanced time series approach. Energy 2016;116:963–77.
[5] Köne AÇ, Büke T. Forecasting of CO2 emissions from fuel combustion using trend analysis. Renew Sustain Energy Rev 2010;14:2906–15.
[6] Middleton RS, Gupta R, Hyman JD, Viswanathan HS. The shale gas revolution: barriers, sustainability, and emerging opportunities. Appl Energy 2017;199:88–95.
[7] Patzek TW, Male F, Marder M. Gas production in the Barnett Shale obeys a simple scaling theory. Proc Natl Acad Sci USA 2013;110:19731–6.
[8] Lee T, Bocquet L, Coasne B. Activated desorption at heterogeneous interfaces and long-time kinetics of hydrocarbon recovery from nanoporous media. Nat Commun 2016;7:11890.
[9] Chen C. Multiscale imaging, modeling, and principal component analysis of gas transport in shale reservoirs. Fuel 2016;182:761–70.
[10] Ma L, Dowey PJ, Rutter E, Taylor KG, Lee PD. A novel upscaling procedure for characterising heterogeneous shale porosity from nanometer-to millimetre-scale in 3D. Energy 2019;181:1285–97.
[11] Wang H, Chen L, Qu Z, Yin Y, Kang Q, Yu B, et al. Modeling of multi-scale transport phenomena in shale gas production — a critical review. Appl Energy 2020;262:114575.
[12] Zhu Y, Su H, Jing Y, Guo J, Tang J. Methane adsorption on the surface of a model of shale: a density functional theory study. Appl Surf Sci 2016;387:379–84.
[13] Qajar A, Daigle H, Prodanović M. Methane dual-site adsorption in organic-rich shale-gas and coalbed systems. Int J Coal Geol 2015;149:1–8.
[14] Yu H, Fan J, Xia J, Liu H, Wu H. Multiscale gas transport behavior in heterogeneous shale matrix consisting of organic and inorganic nanopores. J Nat Gas Sci Eng 2020;75:103139.
[15] Yang X, Zhou W, Liu X, Yan Y. A multiscale approach for simulation of shale gas transport in organic nanopores. Energy 2020;210:118547.
[16] Mehmani A, Prodanović M, Javadpour F. Multiscale, multiphysics network modeling of shale matrix gas flows. Transport Porous Media 2013;99:377–90.
[17] Javadpour F. Nanopores and apparent permeability of gas flow in mudrocks (shales and siltstone). J Can Petrol Technol 2009;48:16–21.
[18] Chen W, Yang Y, Wang T. Non-linear gas transport inside an ultra-tight Longmaxi shale core under thermal stimulation conditions. Energy 2019;186:115846.
[19] Darabi H, Ettehad A, Javadpour F, Sepehrnoori K. Gas flow in ultra-tight shale strata. J Fluid Mech 2012;710:641–58.
[20] Cao G, Zhang H, Jiang W, Wu S, Zhu D, Lin M. A new gas content evaluation method for organic-rich shale based on fractionation of carbon isotopes of methane. SPE J 2019:197043.
[21] Akkutlu IY, Fathi E. Multiscale gas transport in shales with local kerogen heterogeneities. SPE J 2012;17:1002–11.
[22] Li W, Liu J, Zeng J, Leong YK, Elsworth D, Tian J, et al. A fully coupled multi-domain and multiphysics model for evaluation of shale gas extraction. Fuel 2020:278.
[23] Cao G, Lin M, Jiang W, Li H, Yi Z, Wu C. A 3D coupled model of organic matter and inorganic matrix for calculating the permeability of shale. Fuel 2017;204:129–43.

[24] Cao G, Lin M, Jiang W, Zhao W, Ji L, Li C, et al. A statistical-coupled model for organic-rich shale gas transport. J Petrol Sci Eng 2018;169:167–83.
[25] Altan A, Hacıoğlu R. Model predictive control of three-axis gimbal system mounted on UAV for real-time target tracking under external disturbances. Mech Syst Signal Process 2020;138:106548.
[26] Karasu S, Altan A, Bekiros S, Ahmad W. A new forecasting model with wrapper-based feature selection approach using multi-objective optimization technique for chaotic crude oil time series. Energy 2020;212:118750.
[27] Idowu NA, Blunt MJ. Pore-scale modelling of rate effects in waterflooding. Transport Porous Media 2010;83:151–69.
[28] Dong H, Blunt MJ. Pore-network extraction from micro-computerized-tomography images. Phys Rev E - Stat Nonlinear Soft Matter Phys 2009;80:036307.
[29] Yi Z, Lin M, Jiang W, Zhang Z, Li H, Gao J. Pore network extraction from pore space images of various porous media systems. Water Resour Res 2017;53:3424–45.
[30] Lee A, Gonzalez M, Eakin B. The viscosity of natural gases. J Petrol Technol 1966;18:997–1000.
[31] Dranchuk P, Abou-Kassem H. Calculation of Z factors for natural gases using equations of state. J Can Petrol Technol 1975;14:4.
[32] Jiang W, Lin M. Molecular dynamics investigation of conversion methods for excess adsorption amount of shale gas. J Nat Gas Sci Eng 2018;49:241–9.
[33] Rexer TFT, Benham MJ, Aplin AC, Thomas KM. Methane adsorption on shale under simulated geological temperature and pressure conditions. Energy Fuel 2013;27:3099.
[34] Balhoff MT, Thomas SG, Wheeler MF. Mortar coupling and upscaling of pore-scale models. Comput Geosci 2008;12:15–27.
[35] Cui X, Bustin AMM, Bustin RM. Measurements of gas permeability and diffusivity of tight reservoir rocks: different approaches and their applications. Geofluids 2009;9:208–23.
[36] Ji L, Lin M, Jiang W, Wu C. An improved method for reconstructing the digital core model of heterogeneous porous media. Transport Porous Media 2017;121:389–406.